Focus quality in raster-scan imaging via a multimode fiber

ZHOUPING LYU,[1,2,*] GERWIN OSNABRUGGE,[1] PEPIJN W. H. PINKSE,[3] AND LYUBOV V. AMITONOVA[1,2]

[1]*Advanced Research Center for Nanolithography (ARCNL), Science Park 106, 1098 XG, Amsterdam, The Netherlands*
[2]*LaserLaB, Department of Physics and Astronomy, Vrije Universiteit Amsterdam, De Boelelaan 1081, 1081 HV Amsterdam, The Netherlands*
[3]*MESA+ Institute for Nanotechnology, University of Twente, P.O. Box 217, 7500 AE Enschede, The Netherlands*
Corresponding author: z.lyu@arcnl.nl

A multimode fiber (MMF) is a minimally invasive imaging probe. The most popular approach of MMF-based microscopy is raster-scan imaging, where the sample is illuminated by foci optimized on the fiber output facet by wavefront shaping (WFS). Imaging quality can be quantified by characteristic parameters of the optimized spots. We investigate the influence of the input light position on WFS through a round-core MMF with partial mode control, a situation often encountered in real life. We further demonstrate a trade-off between the shape and contrast of the foci generated on the output facet: the center input position is beneficial for high-contrast imaging, while the edge input position helps to reduce focus aberrations. These results are important for high field-of-view raster-scan imaging via an MMF. © 2022 Optica Publishing Group under the terms of the Optica Open Access Publishing Agreement

1. INTRODUCTION

Holographic endomicroscopy is a powerful platform for minimally invasive bioimaging and remote sensing [1–3]. For this method, the light scrambling effects of a multimode fiber (MMF) need to be overcome, which can be achieved by wavefront shaping (WFS) [4]. MMFs support the propagation of thousands of spatial modes within a small cross-sectional area of about 0.01 mm × 0.01 mm and therefore allow microscopy at high spatial information density. The imaging potential of endomicroscopy has already been exploited to visualize neural activity at arbitrary depths in a living brain [5–7]. However, spatial resolution, imaging speed, contrast, and field-of-view (FOV) can be improved further.

The most popular approach of MMF-based endomicroscopy exploits raster-scan imaging [3,6,8]. By WFS, the phase front of the light incident on the fiber is modulated such that constructive interference is achieved at the desired focus location at the fiber output. In order to form an image, a sample is illuminated by a sequence of these focal spots at different locations. The performance of this raster-scan imaging mainly depends on the quality of the generated foci. Ideally, a perfect diffraction-limited focal spot should be generated at any point at the fiber output facet. Control of a large fraction of modes is essential for nonaberrated foci [9]. The highest fraction of optical power in a single spot can be achieved by oversampling (the number of controls higher than the number of fiber modes [6,10]). However, for a field-of-view of only 200 μm in diameter, this would require the control of about $34 \cdot 10^3$ phase segments,

which will lead to a long optimization time and require a spatial light modulator with a large number of pixels. Image quality can also be improved by the use of MMF with a square core, which was found to be superior to the more traditional round core since the eigenmodes of the square-core fiber fill out the core more uniformly [11]. Computational algorithms can increase image quality by modeling a spatially variant point-spread function and performing deconvolution [12].

Here, we investigate the performance of a round-core MMF-based endoscope with partial mode control, which is characteristic for a situation with a large-core MMF and a finite number of controlled pixels of a round illumination beam in its Fourier plane. We use phase-only modulation, conventional fibers, and a common Fourier plane configuration [6,13,14]. We show that, counterintuitively, coupling the input light to the center of the MMF is not always the best strategy. We show the trade-off between the shape and contrast of the generated focal spots. The center input position is beneficial for high contrast, while edge input positions help to reduce aberrations.

2. EXPERIMENTAL SETUP

The experimental setup is presented schematically in Fig. 1(a). We use a diode-pumped continuous wave (CW) laser with a wavelength of 532 nm. A half-wave plate (HWP), a polarizing beam splitter (PBS), and a beam blocker are used to modulate the beam power. Two achromatic doublets L₁ (focal length, $f_1 = 50$ mm) and L₂($f_2 = 150$ mm) form a telescope to
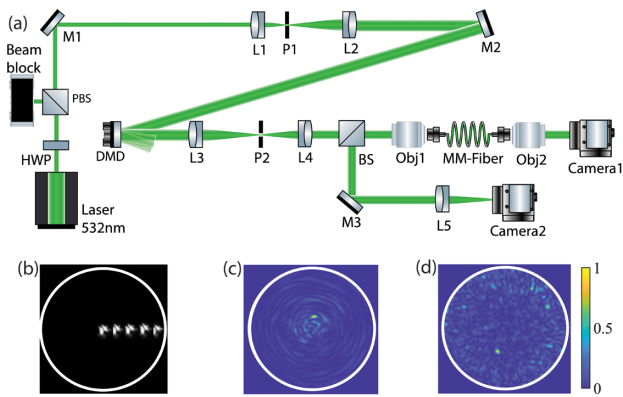
Fig. 1. (a) Experimental setup (HWP, half-wave plate; PBS, polarizing beam splitter; M, mirror; L, lens; P, pinhole; DMD, digital micromirror device; BS, beam splitter; Obj, objective; MMF, multi-mode fiber. (b) Examples of the input fields before WFS at different input positions with zero phase on the DMD. (c), (d) Output speckle patterns measured without WFS for the input beams at (c) $d_{in} = 0.1r$ and (d) $d_{in} = 0.9r$.

Fig. 2. (a) Example of the optimized phase pattern created by using 254 DMD segments for the input beams at $d_{in} = 0.1r$, r = 25 μm. (b) Sum of 10 foci optimized with the same parameter. Black circle shows the fiber core. (c) Zoomed-in foci at a distance of 0 μm (left), 15 μm (center), and 22.5 μm (right) from the fiber center. The corresponding ellipticities are 0.11 (left), 0.29 (middle), and 0.59 (right). The scale bar is 2 μm.

expand the beam incident at the digital micromirror device (DMD) from Texas Instruments driven by the DLP V-9501 VIS module (Vialux). The DMD phase pattern is imaged on the back focal plane of Objective #1 (Olympus, 20×, NA = 0.4) by a 4 f system consisting of lenses $L_3(f_3 = 150$ mm) and $L_4(f_4 = 100$ mm). The pinhole (P_2) only allows the +1st diffraction order of the DMD to pass. Objective #1 couples light to an MMF. We use a round-core step-index multimode fiber with a diameter of 50 μm and an NA of 0.22 (Thorlabs). The fiber length is around 30 cm. Objective #2 (Olympus, 20×, NA = 0.4) images the fiber output on Camera #1. A beam splitter (BS) between Objective #1 and lens L_4 images the input facet of the MMF on Camera #2 with Objective #1 and lens L_5 ($f_5 = 70$ mm) placed in 4 f configuration.

The DMD consists of 1920 × 1080 tilting micromirrors, which are arranged on a rectangular grid. Each micromirror can individually rotate to +12°, the "on state," or to −12°, the "off state." We use the Lee hologram method to generate desired wavefronts [15]. Micromirrors are grouped together to form square segments consisting of 13 × 13 to 55 × 55 elements. Within each DMD segment, a binary 2D grating is created. Displacement of the "on state" and the "off state" lines of a grating within a segment provides the desired phase shift of the segment. The active area of the DMD has been restricted to a maximum of 550 × 550 micromirrors. This area has been experimentally chosen by measuring the contribution of each segment into the output field. With a fixed maximum of 550 × 550 micromirrors, the more segments we have, the smaller the size of each segment. As a result, after WFS, the light from a single segment will cover a larger portion of the fiber input facet when we use more DMD segments because of the Fourier transformation by the lens.

In the experiments, the position of the input light on the fiber input facet is controlled by the direction of beam propagation after the DMD. Changing the DMD grating's periodicity leads to a change in the light direction. We use five input positions with the distance between the center of the core and the center of the input beam d_{in} varied from 0.1r to 0.9r, where r is the fiber
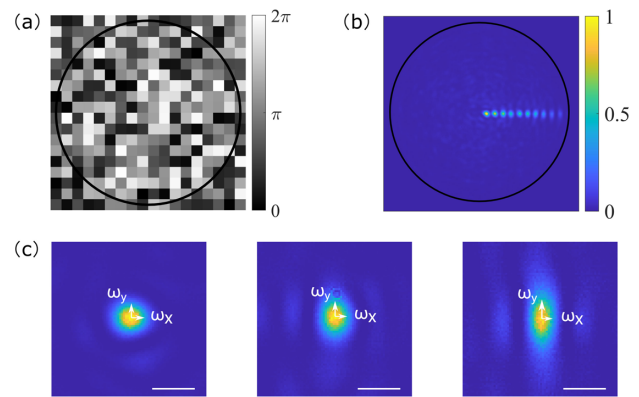
core radius (25 μm). Figure 1(b) shows the sum of five input fields before WFS with a flat phase pattern on the DMD. The input field has a butterfly shape instead of an ideal Gaussian shape because of the aberrations introduced by the not perfectly flat DMD surface and other optical components. The white circle indicates the fiber core. Figures 1(c) and 1(d) show the output speckles measured without WFS for the input beams at $d_{in} = 0.1r$ and $d_{in} = 0.9r$, respectively. For each input position, we generate focal spots on the fiber output facet by the stepwise sequential WFS algorithm [16]. The phase of each segment has been stepped through three equidistant points (0, $2\pi/3$, and $4\pi/3$), while the intensity in the desired region is measured. We calculate the optimal phase by fitting the data with a cosine function. An example of an optimized phase pattern created by using 254 DMD segments for the input beams at $d_{in} = 0.1r$, $r = 25$ μm is shown in Fig. 2(a). The black circle shows the fiber core.

The most time-consuming step for a 2D wavefront optimization is recording the target intensity by a camera. The optimization time is linearly increasing with N_{seg}. We use a camera (Basler acA2440-75μmMED) with a frame rate of 75 Hz. Therefore, 40 ms is required to optimize a single DMD segment, or ∼1500 segments can be optimized per minute.

3. RESULTS AND DISCUSSION

To investigate the influence of the light input position, we couple light to the MMF at different locations and perform the WFS experiments. Five input positions $d_{in} = [0.1r, 0.3r, 0.5r, 0.7r, 0.9r]$ are investigated. For each input position, 50 foci are generated sequentially along a single line on the fiber output facet. The controlled number of segments on the DMD in the experiment varies from 10^2 to 41^2. The square DMD pattern overfills the incident circular beam; thus, we correct the effective number of contributing segments with a factor of $\frac{\pi}{4}$. Hence, a number of DMD segments (N_{seg}) varying from $\frac{\pi}{4} \cdot 10^2$ to $\frac{\pi}{4} \cdot 41^2$ has been investigated. Figure 2(b) shows 10 foci optimized on the fiber output

facet with $N_{seg} = 254$. The optimization has been done with $d_{in} = 0.1r$. Figure 2(c) shows three zoomed-in foci optimized at the center of the fiber (left) and at a distance of 15 μm (center) and 22.5 μm (right) from the fiber center. We see that the shape and intensity of the focal spots change with the position on the output facet. The focal spots become more elongated with increasing distance to the fiber center.

For a quantitative analysis, we fit each generated focal spot with a 2D Gaussian function and calculate the width of a focal spot along the short ($2w_{min}$) and along the long ($2w_{max}$) main axes at half maximum. The focus shape is characterized by the ellipticity $\varepsilon = 1 - w_{min}/w_{max}$. The power in the focal spot is characterized by a power ratio (PR) $= I_{foc}/I_{tot}$, where I_{tot} is the total power at the fiber output facet, and I_{foc} is the power inside the elliptical area around the peak with w_{min} and w_{max} main axes of the ellipse. The focus ellipticity ε and the power ratio PR are measured for a varying number of DMD segments N_{seg} and input beam position d_{in}. The full measurement data set is shown in Appendix A.

Figures 3(a)–3(d) show the ellipticity ε, the power ratio PR, and the widths of the focal spot ($2w_{min}$ and $2w_{max}$) along the main axes as functions of N_{seg}. The signal is averaged over all 50 foci generated at the fiber output facet. Different colors correspond to different coupling positions of the input beam with reference to the fiber center: $d_{in} = 0.1r$ (black line), $0.3r$ (blue line), $0.5r$ (green line), $0.7r$ (red line), and $0.9r$ (magenta line). All the curves for the ellipticity ε and the power ratio PR saturate when the number of segments reaches 1200. This is approximately equal to the total number of modes supported by the MMF for one polarization. However, it is not always possible to control a large fraction of modes, especially if the fiber core (and the resulting FOV) is getting larger. For example, for a fiber with a core diameter of 500 μm and NA $= 0.8$ at wavelength 532 nm, we would need to control around 10^7 modes for two polarizations, whereas the typical SLM has only around 10^6 pixels.

We see that important characteristics of the optimized foci such as the shape and the power ratio crucially depend on the beam position on the fiber input. The focus width along the short axis ($2w_{min}$) does not show a notable change with N_{seg}, as shown in Fig. 3(c), while the width along the long axis ($2w_{max}$) converges to the diffraction limit only for a high N_{seg} [see Fig. 3(d)]. This effect is more pronounced for the central light coupling. To obtain a good focal shape with a relatively low number of segments and, consequently, reduce the aberrations in raster-scan imaging, through a round-core fiber, we need to couple light closer to the core's edge [red and magenta curves in Fig. 3(a)]. On the other hand, results presented in Fig. 3(b) demonstrate that the central coupling provides more power to the focus, which yields better imaging contrast.

Our experiments demonstrate a trade-off between imaging contrast and aberration in raster-scan imaging through a round-core MMF. Additionally, we investigate this trade-off for different parameters of fiber length, diameter, and working distance through numerical modeling. We simulate light propagation in a round-core multimode fiber with the same setup configuration. The stepwise WFS algorithm in the experiment is an iterative algorithm, which changes the wavefront as set by the DMD to optimize the focus at the target plane. In the
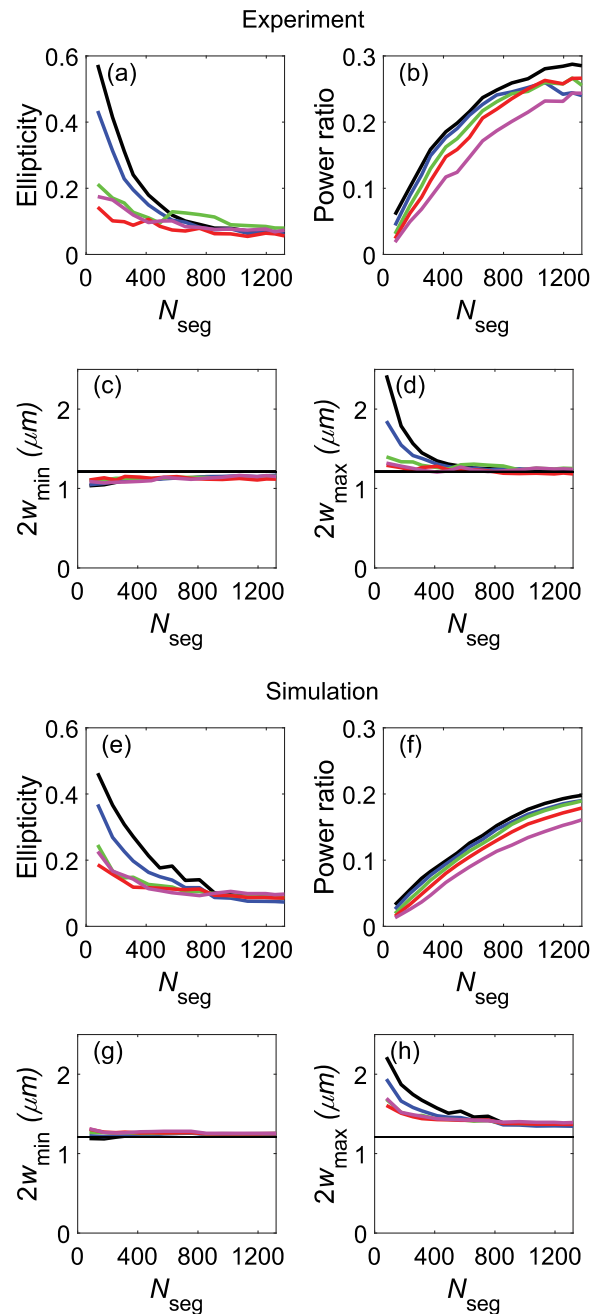

Fig. 3. (a) Experimentally measured ellipticity ε, (b) power ratio PR, (c) beam waists $2w_{min}$, and (d) $2w_{max}$ averaged over 50 foci distributed over output facet as a function of the number of segments (N_{seg}) on the DMD. Results of semianalytical simulations: (e) ε, (f) PR, (g) $2w_{min}$, and (h) $2w_{max}$ averaged over 50 foci distributed over output facet as a function of N_{seg}. Different colors correspond to different distances between the input beam and the fiber center: $d_{in} = 0.1r$ (black line), $0.3r$ (blue line), $0.5r$ (green line), $0.7r$ (red line), and $0.9r$ (magenta line). The black lines show the diffraction limit of 1.21 μm.

simulation, we separate the calculation of one propagation cycle into three substeps. First, we model the light propagation from DMD to the fiber assuming perfect relay optics. Second, we simulate the propagation through an ideal multimode fiber using a semianalytical mode-solver [17]. This solver calculates the fiber modes (for both polarizations) and their corresponding

propagation constants for a given fiber geometry. The propagation of any input field $E_{in}(x, y)$ through a fiber of length L to output field $E_{out}(x, y)$ is then given by Eq. (1):

$$E_{out}(x, y) = \sum_{k}^{N} \alpha_k E_k(x, y) e^{-i\beta_k L}, \qquad \textbf{(1)}$$

where (x, y) are the spatial coordinates, L is the length of the fiber, $E_k(x, y)$ is the normalized kth- fiber mode, β_k is the propagation constant of the kth- mode, and α_k is the overlap integral between the normalized kth- mode and the input field $E_{in}(x, y)$. For the simple round-core step-index fiber, the analytical solution of the wave equation provides guided modes $E_k(x, y)$, which are combinations of Bessel functions [17]. To reduce computing requirements, the grid spacing for guided modes $E_k(x, y)$ is limited to the NA of the round-core step-index fiber. Finally, free propagation from fiber output facet to image plane was introduced to the model. Free propagation is done by the angular spectrum propagation method. The propagated field is calculated as the sum of weighted plane waves with different phase shifts [18]. The field-of-view expands according to the working distance.

The simulation of the stepwise WFS algorithm follows the same steps as described in Section 2. The input field $E_{in}(x, y)$ is assumed to be a plane wave and is divided into segments. The target intensity is recorded when each segment is swept through $(0, 2\pi/3,$ and $4\pi/3)$. The optimal phase pattern for this segment is calculated by fitting the intensity as a cosine function of phase. After going through all the segments, the optimized wavefront for each focus spot is updated individually. As a result, 50 focus spots at the fiber output for one input position have been simulated for a different number of segments. Both the ellipticity ε and power ratio PR are also averaged over all 50 foci generated at the fiber output facet. This process is repeated for five different positions $0.1r$ to $0.9r$ by shifting the input field $E_{in}(x, y)$, where r is the fiber core radius.

The simulation results with the same parameters as in the experiment are shown in Figs. 3(e)–3(h). Different colors correspond to different distances between the input beam and the fiber center: $d_{in} = 0.1r$ (black line), $0.3r$ (blue line), $0.5r$ (green line), $0.7r$ (red line), and $0.9r$ (magenta line). Our semianalytical simulations also show that the shape and power ratio are determined by the position of the input beam. To obtain a good shape, we need to couple light closer to the core edge [red and magenta curves in Fig. 3(e)]. On the other hand, the central coupling provides higher power in the focus [black curve in Fig. 3(f)]. Therefore, to improve imaging contrast, input close to the fiber core center is preferable. The saturation value of the enhancement from the experiment is a bit higher than the simulation. It can be explained by the limited dynamic range of the camera and underestimated background. Another reason could be fiber bending that leads to mode coupling, which is neglected in the simulation.

We use our simulation model to investigate the trade-off between the shape and power ratio for different parameters: shape of the input beam, fiber length, fiber diameter, and working distance. The experimental and simulation results are summarized in Figs. 4(a) and 4(b), respectively; the detailed description of the simulated data is given in Appendix B. In
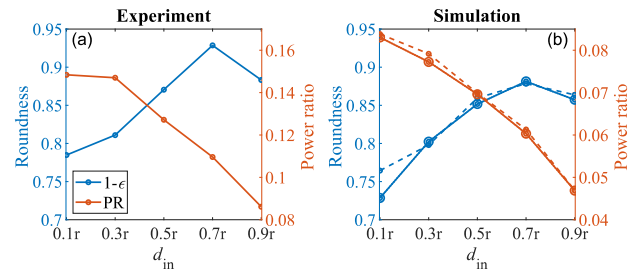

Fig. 4.   (a) Experimental and (b) simulated data for roundness, $1 - \varepsilon$ (blue), and power ratio, PR (orange), averaged over 50 foci uniformly distributed on the fiber output facet and optimized by 314 DMD segments as a function of the input beam position (d_{in}). The solid lines show results for the fiber core of 50 µm, fiber length of 30 cm (or 1 m) and plane wave on the DMD. Dashed lines show the results of simulation for a Gaussian beam on the DMD.

Fig. 4, the roundness (which is calculated by $1 - \varepsilon$) and the power ratio, PR, averaged over 50 foci uniformly distributed over the fiber output and optimized by 314 segments on the DMD are plotted as a function of input position (d_{in}). The solid lines show results for a 50 µm fiber core, fiber length of 30 cm, and plane-wave DMD illumination. Simulations for 1 m fiber length show exactly the same results as for fiber length of 30 cm. The dashed line in Fig. 4(b) shows the simulation results for a Gaussian beam on the DMD. Experiments and simulations demonstrate that the roundness improves and the power ratio reduces with d_{in} closer to the edge. Simulations confirm that the trade-off between the round shape and the intensity of the foci is present for different shapes of the input beam, fiber lengths, and the core diameter, as presented in Appendix B, Fig. 6 for a MMF with 105 µm core. The simulation was also performed for imaging planes located at 100 and 200 µm away from the fiber output facet. The result is shown in Appendix B, Fig. 7. Similar to the previous results, we see that a higher intensity corresponds to a central input position, while coupling light closer to the edge helps to provide a better shape. Thus, the trade-off between aberration and intensity remains in force for imaging at a distance from the fiber facet.

To summarize, we have experimentally demonstrated the trade-off between the shape and the relative intensity of the focal spots generated on the output facet of a round-core MMF. We show that, in the case of a low number of controlled segments, coupling the input beam to the fiber center can be used to improve imaging contrast, while coupling to the fiber edge can be used to reduce aberrations. Input positions around $0.5 - 0.7r$ allow for good balance between focus contrast and shape. The aberrations can be corrected by postprocessing; however, it requires a complicated approach and an additional precalibration step since standard deconvolution algorithms work for a uniform point-spread function [12,19,20]. The semianalytical simulations confirm our experimental findings and reveal the existence of the trade-off for different experimental conditions. State-of-the-art MMF-based endoscopes have a FOV of only 50 µm in diameter. Our research shows how a larger FOV can be reached with a larger-core MMF while only controlling a subset of the fiber modes.

APPENDIX A: EXPERIMENTAL DATA OF ELLIPTICITY AND POWER RATIO

This appendix presents the measured ellipticity ε and power ratio PR for three different input positions d_{in} as a function of DMD segments N_{seg} and distance between the fiber center and the optimized focal spot on the fiber output facet (d_f).

The ellipticity and power ratio of 50 foci at output facet with N_{seg} from $\pi/4 \cdot 10^2$ to $\pi/4 \cdot 41^2$ for three different input positions ($d_{in} = 0.1r, 0.5r, 0.9r$) are presented in Fig. 5. The first column illustrates the input fiber facet. The small black dots indicate the center positions of the input beam. The white and red circles show the minimum and maximum sizes of the input beam after WFS with $N_{seg} = \pi/4 \cdot 10^2$ and $N_{seg} = \pi/4 \cdot 41^2$ active segments on the DMD, respectively. The second column shows the ellipticity of the optimized foci, ε, as a function of the number of controlled segments on the DMD (N_{seg}) and the distance between the fiber center and the optimized focal spot on the fiber output facet (d_f). The ellipticity ε is close to 0 when the generated focus has a nearly perfect shape and is about 1 when the focus is elongated. The third column represents the power ratio, PR, as a function of N_{seg} and d_f. Note the color bars for the second and third columns are reversed. The yellow color indicates good performance: good shape and high intensity. We perform phase-only modulation and control only a single polarization, which results in the relatively low values for the PR.

When the input light is coupled to the fiber center, the shape of the optimized foci on the output facet depends on the number of controlled segments. For a low N_{seg}, the round shape can be achieved only within the $d_f = 5$ μm region [see Fig. 5(a)]. Foci
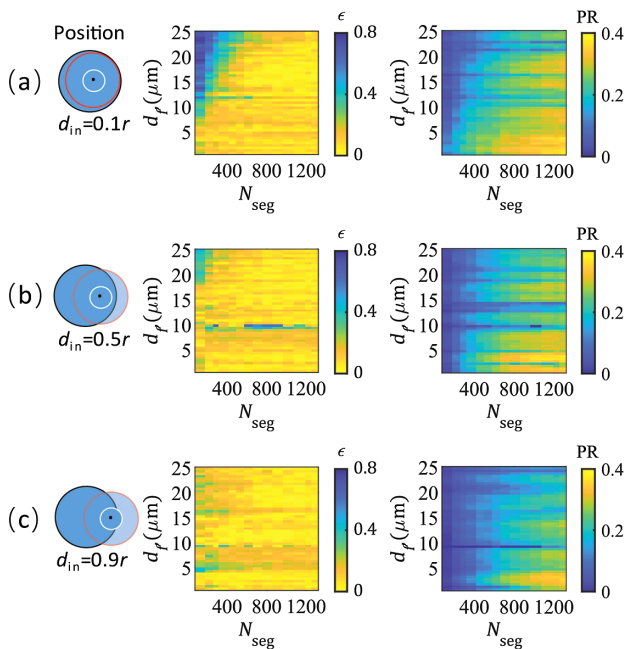
generated close to the edge have an elongated shape with ε up to 0.8. The reason is that a different number of fiber modes effectively contributed to the generation of foci at different target positions. Compared with foci located at the edge of the core, a relatively smaller fraction of fiber modes contributes to the foci around the center of the output facet [8]. Thus, fewer segments should suffice to offer a diffraction-limited focal spot with high contrast at the center of the output facet. Similarly, to generate a focal spot near the edge of output facet, we need more segments. This explains the high ellipticity (blue area) on the top left corner in Fig. 5(a) middle column. However, the blue part shrinks if the input beam approaches the edge of the core. As shown in Fig. 5(c), a nearly perfect focus shape with low ellipticity can be achieved independent of the number of segments or positions of the optimized foci by an input beam closer to the edge of the MMF core. This is because the greater variety of fiber modes is addressed by such an input. As shown in Figs. 1(c) and 1(d), when $d_{in} = 0.1r$, the output pattern without wavefront shaping shows elongated rings, while the unoptimized output for edge input positions shows a more complete speckle pattern with a finer and more homogeneous structure. Compared with the elongated speckles for the center input position, the more random, finer structure for the edge input position is a better initial condition for generating a focal spot. Clearly, to improve the shape of the foci for a low number of controlled segments, the edge input position should be used.

The power ratio in the optimized spot at the fiber output increases with the number of segments, as predicted by WFS theory [4], for any input position. However, in contrast with the focal shape, the maximal PR reduces when the input position approaches the fiber edge (see the third column of Fig. 5). The reason is that, for an input position closer to the fiber edge, more control power is lost, as shown in the first column of Fig. 5. When $d_{in} = 0.1r$, almost all light is coupled to the fiber for different N_{seg}. When $d_{in} = 0.5r$, a part of the light is lost for high N_{seg}. When $d_{in} = 0.9r$, we lose light even with low N_{seg}. Obviously, to improve PR for a low number of controlled segments, the center input position should be used.

The horizontal stripes in Fig. 5(b) originate from "blind spots" of WFS [1]. During WFS, the reference field is a speckle pattern. Because of the well-known exponential distribution of the intensity of fiber speckles, some positions have relatively low intensity where WFS fails. The power ratios fit to these failed foci will be lower than normal, but the ellipticities follow that of the original speckles.

Fig. 5. Ellipticity ε (central column) and the power ratio PR (right column) of a generated focus on the fiber output facet as a function of the number of segments on the DMD (N_{seg}) and the distance between the fiber center and the position of the optimized spot (d_f) for light coupled to the MMF at a distance about (a) $0.1r$, (b) $0.5r$, and (c) $0.9r$ as illustrated in the left column. White and red circles in the first column show the minimum and maximum sizes of the input beam after WFS, respectively. Yellow indicates good performance.

APPENDIX B: SIMULATIONS OF WFS THROUGH AN MMF FOR DIFFERENT PARAMETERS

Here, we show the simulation results for different parameters: input beam shape, length, diameter, and imaging distance from the fiber facet. In the first set of simulations, we use our model to simulate WFS in an MMF with a core diameter of 50 μm and length of 30 cm. Instead of plane wave illumination on the DMD, we simulate a Gaussian beam with an FWHM of 10 cm. The results are shown in Figs. 6(a) and 6(b). There is no perceptible difference between the plane wave [Figs. 3(e)–3(h)] and Gaussian inputs.
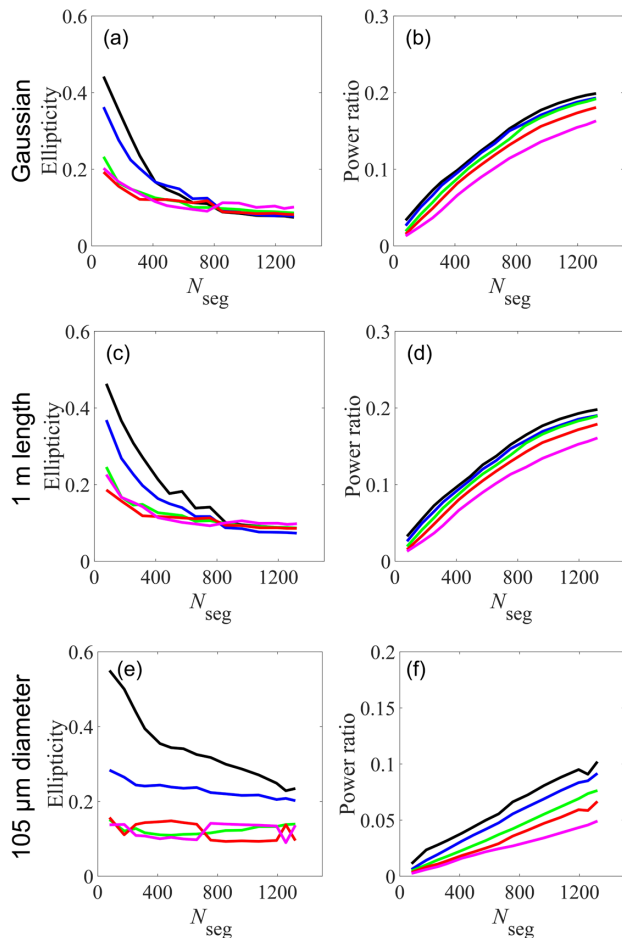
Fig. 6. Semianalytical simulation of the ellipticity ε and the PR averaged over 50 foci as a function of the number of segments for different parameters: Gaussian input beam, fiber with 1 m length, fiber with 105 μm diameter. Different colors correspond to different coupling distances between the input beam and the fiber center: $d_{in} = 0.1r$ (black line), $0.3r$ (blue line), $0.5r$ (green line), $0.7r$ (red line), and $0.9r$ (magenta line).

Fig. 7. Semianalytical simulation of the power ratio PR and $2w_{min}$ averaged over 50 foci at a distance of 100 and 200 μm to the fiber facet as a function of N_{seg} for a fiber with 50 μm diameter and 30 cm length with a plane-wave input. Different colors correspond to different coupling distances between the input beam and the fiber center: $d_{in} = 0.1r$ (black line), $0.3r$ (blue line), $0.5r$ (green line), $0.7r$ (red line), and $0.9r$ (magenta line). The horizontal black line at (b), (d) is the diffraction limit at the fiber facet.

In the next set of simulations, we use our model to investigate the influence of fiber length and simulate WFS in an MMF with a core diameter of 50 μm, with different lengths and with a plane wave input. The results for 1 m MMF presented in Figs. 6(c) and 6(d) show the expected behavior.

In the next set of simulations, we use our model to investigate the influence of a fiber core diameter. We simulated WFS in an MMF with a length of 1 m, different core diameters, and plane wave as an input. The results for the MMF with a 105 μm core are presented in Figs. 6(e) and 6(f). Compared with 50 μm fiber diameter [presented in Figs. 3(e)–3(h)], 105 μm diameter fiber shows more pronounced dependence on the beam shape and power ratio from input beam positions (d_{in}). The reason is that the MMF with a 105 μm core has four times as many guided modes as an MMF with a core of 50 μm.

In the final set of simulations, we check if the trade-off between aberration and intensity remains valid for focusing at a distance from the output fiber facet. We simulated WFS in an MMF with a core diameter of 50 μm, length of 30 cm, and plane-wave input. Foci have been optimized at a distance of 100
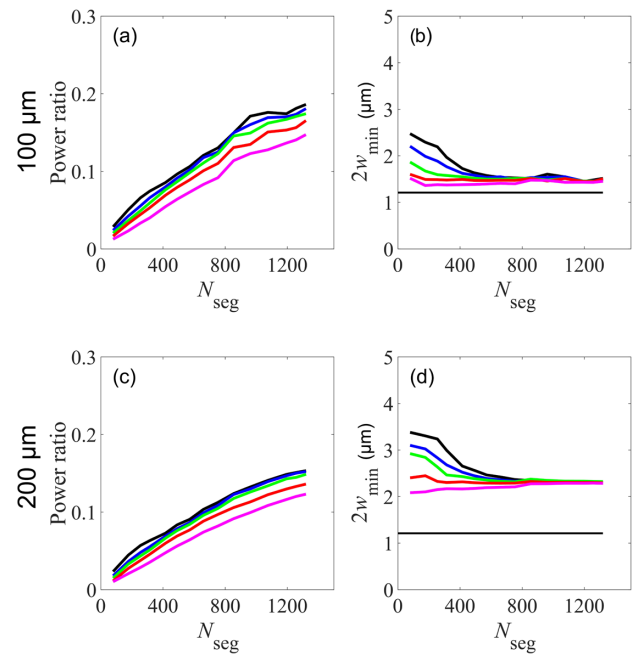
μm [see Figs. 7(a) and 7(b)] and 200 μm [see Figs. 7(c) and 7(d)] from the output fiber facet. The field-of-view expands according to the free-space propagation and the distance of target foci to the axis d_f changes accordingly. The power ratio shows the same trend as before: the closer the input position to the center of fiber, the higher the intensity. The minimal beam waist ($2w_{min}$) decreases as d_{in} goes to the fiber edge, which means the aberration caused by low N_{seg} reduces. Therefore, we can conclude that the trade-off between aberration and intensity remains in place for focusing at a distance from the output MMF facet.

Disclosures. The authors declare no conflicts of interest.

Data availability. Data underlying the results presented in this paper are not publicly available at this time but may be obtained from the authors upon reasonable request.

REFERENCES

1. T. Čižmár and K. Dholakia, "Shaping the light transmission through a multimode optical fibre: complex transformation analysis and applications in biophotonics," Opt. Express **19**, 18871–18884 (2011).
2. R. Di Leonardo and S. Bianchi, "Hologram transmission through multi-mode optical fibers," Opt. Express **19**, 247–254 (2011).

3. T. Čižmár and K. Dholakia, "Exploiting multimode waveguides for pure fibre-based imaging," Nat. Commun. **3**, 1027 (2012).

4. I. M. Vellekoop and A. P. Mosk, "Focusing coherent light through opaque strongly scattering media," Opt. Lett. **32**, 2309–2311 (2007).

5. S. Ohayon, A. Caravaca-Aguirre, R. Piestun, and J. J. DiCarlo, "Minimally invasive multimode optical fiber microendoscope for deep brain fluorescence imaging," Biomed. Opt. Express **9**, 1492–1509 (2018).

6. S. Turtaev, I. T. Leite, T. Altwegg-Boussac, J. M. P. Pakan, N. L. Rochefort, and T. Čižmár, "High-fidelity multimode fibre-based endoscopy for deep brain in vivo imaging," Light Sci. Appl. **7**, 92 (2018).

7. S. A. Vasquez-Lopez, R. Turcotte, V. Koren, M. Plöschner, Z. Padamsey, M. J. Booth, T. Čižmár, and N. J. Emptage, "Subcellular spatial resolution achieved for deep-brain imaging in vivo using a minimally invasive multimode fiber," Light Sci. Appl. **7**, 110 (2018).

8. L. V. Amitonova, A. Descloux, J. Petschulat, M. H. Frosz, G. Ahmed, F. Babic, X. Jiang, A. P. Mosk, P. St. J. Russell, and P. W. H. Pinkse, "High-resolution wavefront shaping with a photonic crystal fiber for multimode fiber imaging," Opt. Lett. **41**, 497–500 (2016).

9. A. Descloux, L. V. Amitonova, and P. W. H. Pinkse, "Aberrations of the point spread function of a multimode fiber due to partial mode excitation," Opt. Express **24**, 18501–18512 (2016).

10. I. T. Leite, S. Turtaev, D. E. Boonzajer Flaes, and T. Čižmár, "Observing distant objects with a multimode fiber-based holographic endoscope," APL Photon. **6**, 036112 (2021).

11. M. C. Velsink, Z. Lyu, P. W. H. Pinkse, and L. V. Amitonova, "Comparison of round- and square-core fibers for sensing, imaging, and spectroscopy," Opt. Express **29**, 6523–6531 (2021).

12. R. Turcotte, E. Sutu, C. C. Schmidt, N. J. Emptage, and M. J. Booth, "Deconvolution for multimode fiber imaging: modeling of spatially variant PSF," Biomed. Opt. Express **11**, 4759–4771 (2020).

13. S. M. Popoff, G. Lerosey, R. Carminati, M. Fink, A. C. Boccara, and S. Gigan, "Measuring the transmission matrix in optics: an approach to the study and control of light propagation in disordered media," Phys. Rev. Lett. **104**, 100601 (2010).

14. A. P. Mosk, A. Lagendijk, G. Lerosey, and M. Fink, "Controlling waves in space and time for imaging and focusing in complex media," Nat. Photonics **6**, 283–292 (2012).

15. W.-H. Lee, "III computer-generated holograms: techniques and applications," Prog. Opt. **16**, 119–232 (1978).

16. I. M. Vellekoop, "Feedback-based wavefront shaping," Opt. Express **23**, 12189–12206 (2015).

17. A. W. Snyder and J. Love, *Optical Waveguide Theory* (Springer, 2012).

18. J. W. Goodman, *Introduction to Fourier Optics* (Roberts & Company, 2005).

19. N. Patwary and C. Preza, "Image restoration for three-dimensional fluorescence microscopy using an orthonormal basis for efficient representation of depth-variant point-spread functions," Biomed. Opt. Express **6**, 3826–3841 (2015).

20. T. Yan, C. J. Richardson, M. Zhang, and A. Gahlmann, "Computational correction of spatially variant optical aberrations in 3D single-molecule localization microscopy," Opt. Express **27**, 12582–12599 (2019).